Toward a BMS_2 Design Framework: Adaptive Data-Driven State-of-Health Estimation for Second-Life Batteries With BIBO Stability Guarantees

Xiaofan Cui, *Member, IEEE*, Muhammad Aadil Khan, *Student Member, IEEE*, Surinder Singh, Ratnesh Sharma, and Simona Onori, *Senior Member, IEEE*

***Abstract*— A key challenge that is currently hindering the widespread use of retired electric vehicle (EV) batteries for second-life (SL) applications is the ability to accurately estimate and monitor their state of health (SOH). SL battery systems can be sourced from different battery packs with a lack of knowledge of their historical usage. Accurate SOH estimation is critical because it enables reliable performance, safety, and optimal utilization of SL batteries, ensuring they meet the requirements of various applications including grid energy storage and backup power. In this work, for in-the-field use of SL batteries, we introduce an online adaptive health estimation approach with the guarantees of bounded-input, bounded-output (BIBO) stability. This method relies exclusively on operational data that can be accessed in real-time from SL batteries. The effectiveness of the proposed approach is shown on a laboratory-aged experimental dataset of retired EV batteries.**

***Index Terms*— Adaptive estimation, batteries, battery management systems (BMS), clustering algorithms, data-driven modeling, machine learning, prognostics and health management, second-life (SL) batteries, sensitivity analysis, state of health (SOH).**

I. Introduction

ACCELERATED adoption of lithium-ion battery (LIB) technology for various applications is pushing the transition toward sustainable energy. Electric vehicles (EVs) are at the forefront of this adoption [1], [2], [3], [4], [5] with some original equipment manufacturers (OEMs) announcing a complete shift toward EV production moving away from internal combustion engine vehicles [6]. While this shift is much needed to address climate change concerns, naturally, this has also increased the pressure on the supply chain for the raw materials needed to manufacture LIBs [7]. To tackle the large demand of raw materials for battery manufacturing, and fully embrace a circular economy paradigm, one promising solution lies in the reuse of EV batteries once they retire from their first life (FL). These batteries are expected to retain approximately 70%–80% of their nominal capacity, and they could be well-suited for low-power applications such as grid energy storage and end-user services, e.g., uninterrupted power supply [8], [9], [10].

The state of health (SOH) measures the battery's overall condition, indicating the extent of capacity or power loss relative to its original specifications. A battery management system (BMS) is an essential component that monitors the battery operation to ensure the battery's safe and efficient operation. In second-life (SL) applications, the SOH monitoring function of BMS takes on additional importance, as it must adapt to the varying conditions and histories of repurposed batteries to maintain reliable performance. In SL batteries, advanced SOH monitoring capability is required to account for the lack of knowledge of historical data and varying conditions of operation. Without reliable SOH information, repurposed batteries may face unexpected failures, inefficiencies, or even safety risks in applications such as grid energy storage [11] or backup power, where performance reliability is paramount [12].

To meet the specific needs of SL batteries, a dedicated battery management system, referred to as BMS_2, is essential [13]. The degradation level of retired batteries significantly depends on their usage history [14]; however, historical data for these batteries are often unavailable [13], [15]. To address this challenge, the proposed online adaptive health estimation method enables the model to adapt to new, real-time data, ensuring accurate SOH estimation without relying on historical usage information or extensive predeployment characterization.

II. Literature Review

Numerous studies have used semiempirical methods [16], [17], [18], [19] and physics-based models [20], [21], [22], [23] for SOH estimation. Semiempirical methods use algebraic

Received 12 July 2024; revised 17 November 2024; accepted 11 December 2024. Date of publication 16 January 2025; date of current version 14 May 2025. This work was supported in part by the StorageX Initiative within the Precourt Institute of Energy, Stanford University; and in part by the University of California, Los Angeles (UCLA), Department of Electrical and Computer Engineering, Faculty Start-Up Fund. An earlier version of this paper was presented in part at the 2024 American Control Conference, Toronto, ON, Canada, in July 2024. *(Corresponding author: Simona Onori.)*

Xiaofan Cui was with the Department of Energy Science and Engineering, Stanford University, Stanford, CA 94305 USA. He is now with the Department of Electrical and Computer Engineering, University of California at Los Angeles, Los Angeles, CA 90095 USA (e-mail: cuixf@seas.ucla.edu).

Muhammad Aadil Khan and Simona Onori are with the Department of Energy Science and Engineering, Stanford University, Stanford, CA 94305 USA (e-mail: maadilk@stanford.edu; sonori@stanford.edu).

Surinder Singh and Ratnesh Sharma are with Relyion Energy Inc., Fremont, CA 94538 USA.

Digital Object Identifier 10.1109/TTE.2025.3530498

TABLE I
COMPARISON OF THE PROPOSED METHOD WITH EXISTING SOH ESTIMATION TECHNIQUES FOR SL BATTERIES

Paper	Publication Month	Model Type	Estimation Method	Computational Efficiency	Model Adaptivity	Theoretical Convergence Guarantee
This Work	Present	Data-Driven	Elastic-Net Regression combined with clustering method	+++	+++	✓
[42]	Oct 2023	Semi-Empirical	Data-driven + Semi-empirical model	+++	+	×
[41]	Aug 2024	Semi-Empirical	Accumulated wear function-based aging model	++	+	×
[43]	Jun 2024	Physics-Based	Adaptive Extended Kalman Filter	++	++	✓
[40]	Aug 2024	Data-Driven	Transfer Learning + Long Short-Term Memory Neural Network	+	+++	×

equations to relate SOH to factors such as time, Ampere-hour (Ah) throughput, operating conditions, and stress factors. While these methods perform well under controlled laboratory conditions, their accuracy often declines when applied in real-world, on-the-field environments [24].

The physics-based model offers detailed insights into a battery's internal states, making it well-suited for extrapolation to previously unobserved operating conditions. It describes battery dynamics through coupled partial differential equations, providing a comprehensive representation of internal processes. However, these models are computationally intensive and require the identification of numerous parameters, along with prior knowledge of specific cell characteristics [20]. While physics-based models are widely applied to new batteries, their use in SL batteries remains limited.

Data-driven models are capable of learning complex battery degradation behaviors from the historical data (e.g., voltage, current, and temperature) and the choice of the model can be adjusted based on the computational resources needed to run these models onboard [25], [26]. SOH estimation using data-driven models has used techniques such as linear regression [27], support vector regression [28], Gaussian process regression [29], and neural networks [30], [31]. Traditionally, the performance of these models tends to deteriorate if the incoming data are out-of-distribution [32] in the sense of being statistically different from the kind of data that were used to train the model.

Health estimation for BMS_2 not only requires online functionality but also demands adaptability. This requires the estimator model to dynamically adjust and evolve as more online measurements become available. In principle, it should enhance the model's generalizability to various operating conditions and unforeseen SL batteries once they are deployed. From a practical standpoint, it is essential for the health estimators to guarantee that the error stays within specific bounds. The existing work around adaptive estimation uses a periodic stream of health indicators by performing reference performance tests (RPTs) and using feedback to update the model [33], [34], [35], [36]. Evidently, this is infeasible for BMS_2 since SL batteries cannot be easily removed from service and diagnosed once they are deployed [33]. Another popular approach adopted for this problem uses transfer learning in which a baseline model is trained using a neural network. Afterward, the initial layers of the model are frozen while the final few layers are retrained on the target domain data [37], [38], [39]. The limitation of transfer learning resides in the target domain used to retrain the model. In field operation, the uncertainty of the incoming data is high and it is difficult to ensure that the model performs consistently.

In this work, we introduce an adaptive SOH estimation method that combines clustering-based estimation with regression-based estimation. By grouping cells based on similar aging behavior, clustering enables the algorithm to handle the high cell-to-cell variability of SL batteries effectively. Moreover, the clustering-based approach enhances robustness by grounding the classification in historical data with a forgetting factor, preventing large deviations that could arise from relying solely on recent data points. The regression-based estimator was chosen due to its ability to capture underlying trends in the battery's degradation process using relatively simple and computationally efficient models. It helps capture long-term degradation trends and performs well during the early phases of battery operation, when clustering may not have enough data points to make reliable classifications. The output from both the estimators is combined using a weighted average by adjusting the weights assigned to each method based on the accumulated data.

Our proposed method shows advantages compared with the existing SOH estimation techniques, as shown in Table I. For instance, many data-driven methods, such as transfer learning with LSTM neural networks [40], suffer from lower computational efficiency due to the complexity of neural networks. In contrast, our method is computationally efficient, making it suitable for real-time applications in SL BMSs. The existing semiempirical and physics-based methods, such as the accumulated wear function-based aging model [41], offer limited adaptability to new data or changing conditions. In addition, some methods lack formal convergence guarantees (e.g., the data-driven + semiempirical model in [42] and the transfer learning + LSTM model in [40]). In contrast, a bounded-input, bounded-output (BIBO) stability guarantee is provided in this article. In summary, our approach represents a robust and balanced solution tailored to the complexities of SL

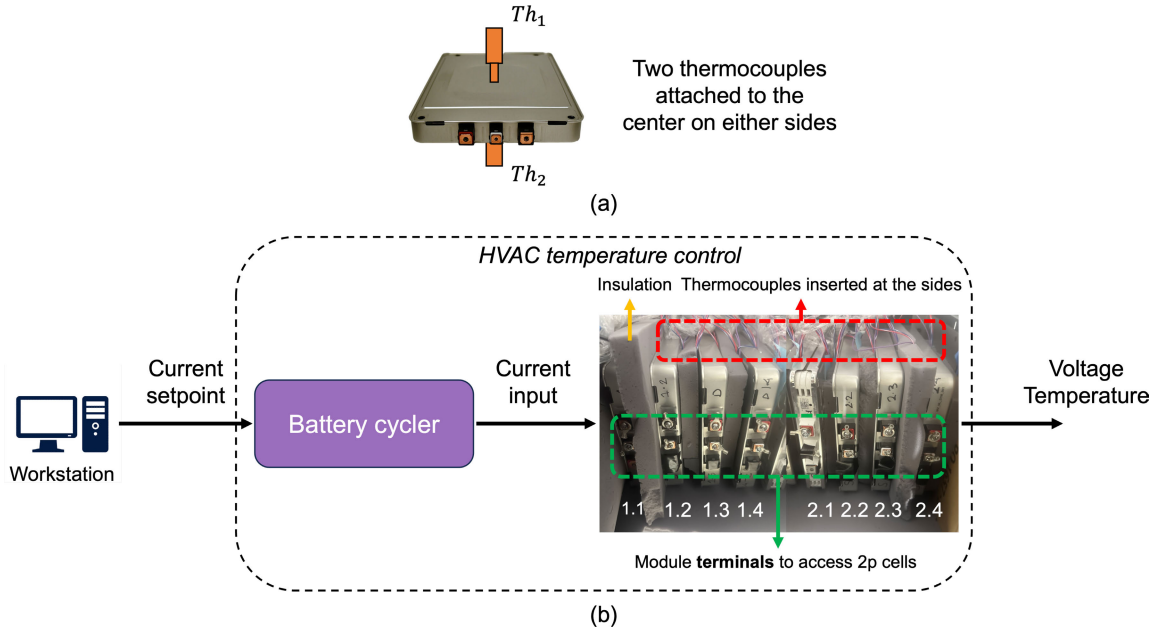

Fig. 1. Experimental setup. (a) Schematic of the two thermocouples Th_1 and Th_2 attached on either side of the module surface to measure the surface temperature. (b) Schematic of the experimental setup showing the battery cycler and eight modules. The modules have insulation between one another and the thermocouples are inserted into the sides of the modules used in this work. On the front, the positive terminal is on the top, the ground terminal is in the middle, and the negative terminal is at the bottom. The workstation is used to set the current setpoint for the battery cycler, which inputs actual current into the modules, and voltage and temperature are measured at the output. The experimental setup is used in an HVAC-controlled laboratory of Relyion Energy located in Santa Clara.

batteries, distinguishing it from the existing SOH estimation techniques.

The rest of this article is organized as follows. Section III presents the retired battery dataset and experimental procedure. The offline data-driven estimator and online adaptive estimator are discussed in Sections IV and V, respectively. The health estimation results on different testing scenarios are illustrated in Section VI. Finally, Section VII concludes this article.

III. Retired Battery Dataset

The dataset used in this work [44] consists of eight retired pouch cells obtained from Nissan Leaf EV battery packs (seven cells from Gen 1 and one from Gen 2)[1] with LMO/graphite chemistry. The nominal capacity (fresh cell) is 33.1 Ah, and the voltage range is from 2.5 to 4.2 V. The cells are arranged in modules where each module contains four pouch cells in a 2s2p configuration accessible via the three terminals outside the module. Based on the module design, a pair of terminals (always including the middle terminal) can be used to access 2p cells while positive and negative terminals together can be used to access the complete 2s2p configuration. In this work, we access only the 2p cells using the positive and middle terminals and refer to these 2p cells as a single cell for the remainder of this article. Hence, the eight cells in the dataset are, in essence, eight 2p cells. The surface temperature of the cells is measured by a pair of thermocouples Th_1 and Th_2 attached to each side of all the modules. The complete experimental setup is shown in Fig. 1. Since these are retired cells with an unknown usage history, it is important to characterize them before starting the aging campaign.

An experimental campaign is designed which consists of three different RPTs and an aging profile repeated multiple times in between RPTs. The cycling profile is designed to mimic the load expected in a grid-storage application in a simplistic manner [45]. The RPTs consist of a C/20 capacity test, a hybrid pulse power characterization (HPPC) test, and a C/40 open-circuit voltage (OCV) test [45]. The C/20 capacity test measures the total capacity of the battery at a slow discharge rate, providing a baseline measurement of its usable capacity and enabling accurate assessment of capacity fade over time. The HPPC test assesses the battery's power capability by applying a sequence of charge and discharge pulses, which helps determine the internal resistance. The OCV test is performed to capture the voltage profile at a low discharge rate.

One important aspect of this experimental campaign is that except for the OCV test performed between 2.5 and 4.2 V, all the other tests are performed between 3 and 4 V. This voltage derating is well-suited for SL applications to guarantee safe operation by limiting the growth of the solid electrolyte interphase (SEI) layer and thereby reducing battery degradation [46].

After the first RPT, cells are cycled within a 3–4-V range according to a synthetic aging protocol, followed by a second RPT, and they continue in this pattern for the remainder of the campaign. The data used in this study were gathered between February 2022 and May 2023. A 1C constant current discharge reflects higher battery utilization during late evening and early night-time hours. Once the SOC reaches 50% (with 100%

[1]Cell 2.1 is from the Nissan Leaf Gen 2 battery pack and the other seven cells are from Gen 1 pack.

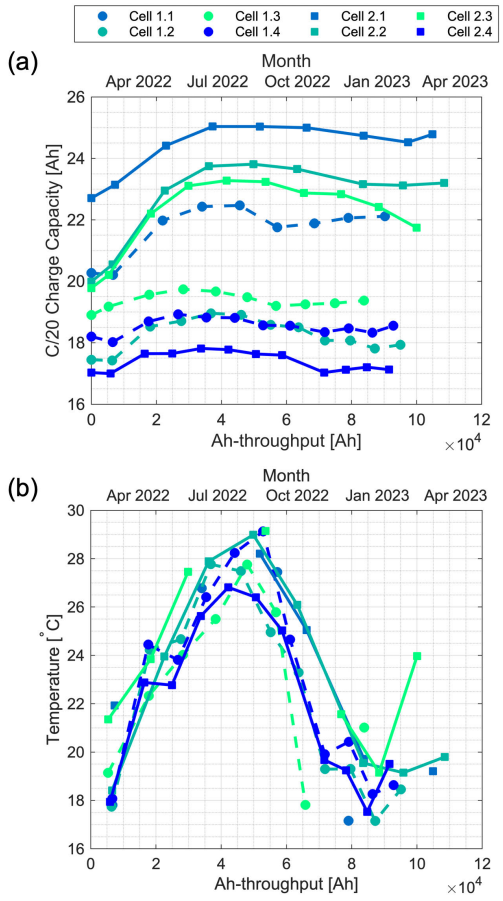

Fig. 2. Capacity and temperature trajectories for the SL cells used in this work. (a) C/20 charge capacity as a function of Ah-throughput (bottom x-axis) and months (upper x-axis). (b) Temperature as a function of Ah-throughput and months with a parabolic shape reaching a maximum value during the months of August/September 2022 indicating the effect of seasonal variation of temperature on all the cells. Gaps in temperature lines represent missing data for those cells, e.g., Cell 2.3.

SOC defined by an upper cutoff of 4 V and 0% SOC by a lower cutoff of 3 V), the C-rate decreases to C/2, indicating lower battery usage for the remainder of the night until the SOC reaches 0% (3 V). Following this, the battery is CC charged at a C/2 rate until it attains 100% SOC (4 V). This entire sequence constitutes one complete operational cycle for the battery.

The initial C/20 charge capacity, determined from the charging phase of the C/20 test, is denoted as $Q_{\text{init,ch,C/20}}$. Similarly, the initial C/20 discharge capacity, obtained from the discharging phase of the C/20 test, is denoted as $Q_{\text{init,disk/20}}$. A small discrepancy is observed between $Q_{\text{init,ch,C/20}}$ and $Q_{\text{init,disk/20}}$. Therefore, $Q_{\text{init,ch,C/20}}$ is selected as the health indicator in this study. The $Q_{\text{init,ch,C/20}}$ trajectories are shown in Fig. 2(a). The capacity degradation is shown with two aligned x-axes: Ah-throughput (cumulative cycling) on the bottom and calendar time (months) on the top. Ah-throughput, as used in this study, refers to the cumulative ampere-hours (Ah) cycled through the battery over time, representing the total charge it has delivered and received. This metric serves as a quantitative measure of the battery's usage intensity and is closely related to its degradation patterns, as increased Ah-throughput typically corresponds with higher levels of capacity fade. Both the axes correspond to the same timeline, providing insights into how degradation progresses as a function of both cycling activity and time. As opposed to conventional battery degradation profiles [47], these cells exhibit an increase in capacity with all the cells reaching a maximum capacity point that is higher than their initial capacities. This behavior is attributed to the variations in cell surface temperature observed throughout the experimental campaign [see Fig. 2(b)]. These fluctuations stem from seasonal changes in ambient temperature in the geographical location where the experiments were conducted. The dataset, being the first of its kind, highlights how cells can potentially behave when used in practical SL applications, in cases where the temperature cannot be controlled. Furthermore, the effect of voltage derating can be observed by the fact that cells, upon reaching the one-year mark from the start of testing, still possess higher or equal capacity compared with their initial capacities.

The following notation is used in the article: sequence $\{a_n\}_{n\leq N} \triangleq \{a_1, a_2, \ldots, a_N\}$ where a_n represents the general term of the sequence $\{a_n\}$, and N represents the length of the sequence. For ease of notation, if not specified, $\{a_n\}$ is equivalent to $\{a_n\}_{n\leq N}$. $\|\cdot\|_2$ represents the $\mathcal{L}^2$-norm. The $\mathcal{L}^2$-norm of a sequence $\{x_n\} = (x_1, x_2, \ldots, x_N)$ is defined by $\|\{x_n\}\|_2 = \sqrt{\sum_{n=1}^{N} x_n^2}$. $\|\cdot\|_\infty$ represents the $\mathcal{L}^\infty$-norm. The $\mathcal{L}^\infty$-norm of a sequence $\{x_n\} = (x_1, x_2, \ldots, x_N)$ is defined by $\|\{x_n\}\|_\infty = \max_{n=1}^{N} |x_n|$. For the remainder of the article, unless otherwise specified, we will denote $\|\cdot\|_\infty$ simply as $\|\cdot\|$. $\mathbb{R}^+$, defined by $\{z \in \mathbb{R} : z > 0\}$, represents the positive real number set. In the remainder of this article, three performance metrics are used: mean absolute percentage error (MAPE), root-mean-squared error (RMSE), and root-mean-squared percentage error (RMSPE), which are defined as

$$\text{MAPE} = \frac{1}{M} \sum_{y\in Y,\ \hat{y}\in\hat{Y}} \frac{|\hat{y}-y|}{y} \times 100\% \tag{1}$$

$$\text{RMSE} = \sqrt{\frac{1}{M} \sum_{y\in Y,\ \hat{y}\in\hat{Y}} (\hat{y}-y)^2} \tag{2}$$

$$\text{RMSPE} = \sqrt{\frac{1}{M} \sum_{y\in Y,\ \hat{y}\in\hat{Y}} \left(\frac{\hat{y}-y}{y}\right)^2} \times 100\% \tag{3}$$

where Y is the measured SOH indicator, $\hat{Y}$ is the SOH indicator from the model estimation, and M is the number of samples.

IV. Offline Data-Driven Model

The SOH for SL batteries is the C/20 charge capacity normalized by their respective initial C/20 capacity at the start of SL.[2] For this work, an elastic-net regression (ENR) model is selected which provides ease of training and adaptability and

[2]Other indicators of SOH, such as the state of energy (SOE), could potentially serve as alternative candidates. Takahashi et al. [29] have shown a high correlation between SOE and SOH for SL batteries.

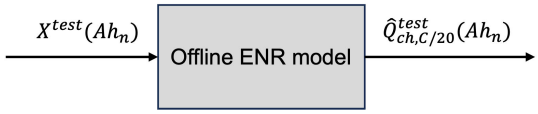

Fig. 3. ENR model with input features X^{test} from the test set and an estimated scalar output $\hat{Q}^{\text{test}}_{\text{ch,C/20}}$ as a function of Ah-throughput.

low computational requirements. The choice of a data-driven model is dictated by the complexity of the data, computational resources, and the training time required to train these models. In our case, another factor that is taken into account is the ease of parameter adaptation when new data become available. In ENR, the loss function used to train the model consists of a linear combination of L_1 (lasso) and L_2 (ridge) regularization terms. The following optimization problem is solved to train the model:

$$\hat{\beta} = \underset{\beta_0,\beta,\lambda}{\arg\min} \; \|Y - X\beta - \beta_0 \mathbf{1}_{n\times 1}\|_2 + \lambda(1-\alpha)\|\beta\|_2^2 + \lambda\alpha\|\beta\|_1 \tag{4}$$

where $Y \in \mathbb{R}^n$ represents the SOH indicators, $X \in \mathbb{R}^{n\times m}$ contains m features each with n observations, $\beta \in \mathbb{R}^m$ contains m regression coefficients, and $\beta_0, \lambda, \alpha \in \mathbb{R}$ are the scalar intercept, the hyperparameter to adjust the influence of L_1 and L_2, and the regularization parameter, respectively.

Fig. 3 shows the flow of data through the offline ENR model where $X^{\text{test}}(\text{Ah}_n)$ represents the input features of the test set at Ah_n and $\hat{Q}^{\text{test}}_{\text{ch,C/20}}(\text{Ah}_n)$ is the estimated C/20 charge capacity. More details about the offline model are given in [45]. Although battery degradation trends are inherently nonlinear over time, our ENR-based health estimation model proves to be effective as it leverages linear approximations between online features and health states. The success of the ENR model indicates that this mapping can be effectively approximated linearly in the feature space, despite the nonlinear time-dependent degradation.

V. Online Adaptive Estimator

The health estimation of BMS_2 not only needs to be online but also adaptive, meaning that the estimator model should adapt and evolve as new online measurements are fed into the BMS_2. The algorithm presented in this article relies on an online feature, referred to as the aging-cycle charge throughput (Q_{age}). In [45], we demonstrated that this feature exhibits a strong correlation with battery health. Here, we briefly revisit this feature

$$Q_{\text{age}}(n) = \int_{t_{\text{ch}}^{\text{age}}(n)}^{t_{\text{dis}}^{\text{age}}(n)} I(t)\,dt \tag{5}$$

where $Q_{\text{age}}(n)$, $t_{\text{ch}}^{\text{age}}(n)$, $t_{\text{dis}}^{\text{age}}(n)$, and $I(t)$ are shown in Fig. 4 and its caption.

Remark 1: Although $I(t)$ is presented in the unit of C-rate in Fig. 4, it must be converted into units of amperes to calculate (5).

The C/20 charge capacity $Q_{\text{ch,C/20}}$ is calculated as

$$Q_{\text{ch,C/20}}(n) = \int_{t_{\text{ch}}^{C/20}(n)}^{t_{\text{dis}}^{C/20}(n)} I(t)\,dt \tag{6}$$

where $Q_{\text{ch,C/20}}(n)$, $t_{\text{ch}}^{C/20}(n)$, $t_{\text{dis}}^{C/20}(n)$, and $I(t)$ are shown in Fig. 4.

Remark 2: This definition is used under controlled RPT conditions, providing a benchmark capacity measure aligned with standard SOH definitions.

Remark 3: Although $I(t)$ is presented in the unit of C-rate in Fig. 4, it must be converted into units of amperes to calculate (6).

The accumulated Ah-throughput for the nth aging cycle Ah_n^{age} is calculated as

$$\text{Ah}_n^{\text{age}} = \int_0^{t_{\text{ch}}^{\text{age}}(n)} \left|I(t)\right| dt. \tag{7}$$

The accumulated Ah-throughput for the aging cycle is calculated by integrating the absolute current from the beginning of the SL period ($t = 0$) up to the time right before the nth aging cycle, denoted by $t_{\text{ch}}^{\text{age}}(n)$. This accumulated Ah-throughput represents the total charge that has flown through the battery since the start of its SL, up to the specified point.

The accumulated Ah-throughput for the nth C/20 charge–discharge cycle $\text{Ah}_n^{\text{ch,C/20}}$ is calculated as

$$\text{Ah}_n^{\text{ch,C/20}} = \int_0^{t_{\text{ch}}^{C/20}(n)} \left|I(t)\right| dt. \tag{8}$$

Similarly, for the nth C/20 cycle, the accumulated Ah-throughput is calculated by integrating the absolute current from the start of the SL period up to the time immediately before the nth C/20 cycle, denoted by $t_{\text{ch}}^{C/20}(n)$.

Definition 1: Given the monotonically increasing accumulated Ah-throughput sequence $\{\text{Ah}_n^{\text{age}}\} = (\text{Ah}_1^{\text{age}}, \text{Ah}_2^{\text{age}}, \ldots, \text{Ah}_N^{\text{age}})$ and the aging-cycle charge throughput sequence $\{Q_{\text{age}}\} = (Q_{\text{age}}(1), Q_{\text{age}}(2), \ldots, Q_{\text{age}}(N))$, then the aging-cycle charge throughput trajectory is a curve denoted by $Q_{\text{age}}(\{\text{Ah}_n^{\text{age}}\})$ or simply Q_{age}.

Definition 2: Given the monotonically increasing accumulated Ah-throughput sequence $\{\text{Ah}_n\} = (\text{Ah}_1^{\text{ch,c/20}}, \text{Ah}_2^{\text{ch,c/20}}, \ldots, \text{Ah}_N^{\text{ch,c/20}})$ and the C/20 charge capacity sequence $\{Q_{\text{ch,C/20}}\} = (Q_{\text{ch,C/20}}(1), Q_{\text{ch,C/20}}(2), \ldots, Q_{\text{ch,C/20}}(N))$, then the C/20 charge capacity trajectory is a curve denoted by $Q_{\text{ch,C/20}}(\{\text{Ah}_n^{\text{ch,c/20}}\})$ or simply $Q_{\text{ch,C/20}}$.

Remark 4: $Q_{\text{ch,C/20}}$ is calculated as shown in Fig. 4. For ease of notation, in the following derivations, the C/20 charge capacity trajectory is simply denoted by $Q(\text{Ah})$.

The normalized SOH indicator is the normalized C/20 charge capacity, calculated by

$$\bar{Q}(\text{Ah}_n) = \frac{Q(\text{Ah}_n)}{Q(0)} \tag{9}$$

where $Q(0)$ is the C/20 charge capacity of the cell measured at the beginning of the SL experiment. For ease of notation, in the following derivations of this section, $Q(0)$ is simply denoted by Q_0.

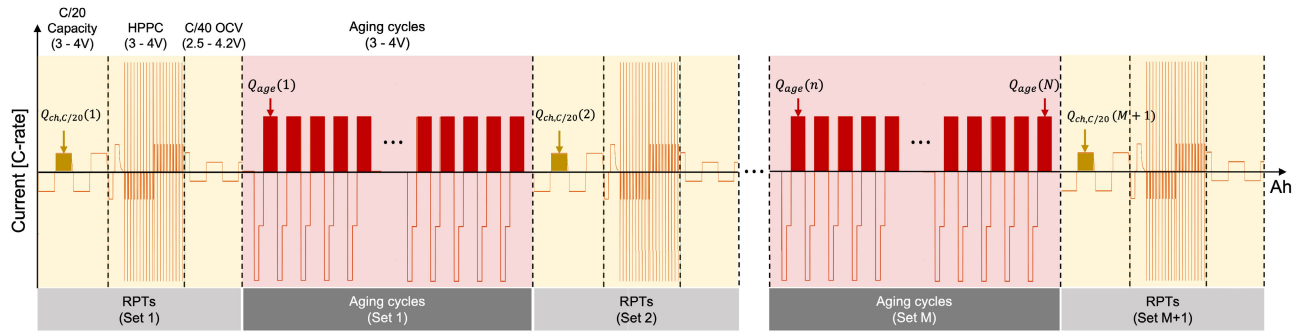

Fig. 4. Design of experiments showing RPTs and aging cycles. RPTs contain C/20 capacity test, HPPC test, and OCV test, which makes one set. For the complete campaign, N sets of aging cycles are performed while $M+1$ sets of RPTs are performed. Within two RPT cycles, hundreds of aging cycles are conducted. Consequently, in this dataset, N is on the order of tens, while M is on the order of thousands. $Q_{\mathrm{ch,C/20}}$, the battery health indicator, is obtained once from the C/20 capacity test of each RPT set, as highlighted in brown. Q_{age}, the aging-cycle charge, is obtained from each cycle, as highlighted in red. The limits of $Q_{\mathrm{ch,C/20}}(i)$ are given by $t_{\mathrm{ch}}^{C/20}(i)$ and $t_{\mathrm{dis}}^{C/20}(i)$ where $i = 1, 2, \ldots, M+1$, and the limits of $Q_{\mathrm{age}}(j)$ are given by $t_{\mathrm{ch}}^{\mathrm{age}}(j)$ and $t_{\mathrm{dis}}^{\mathrm{age}}(j)$ where $j = 1, 2, \ldots, n, \ldots, N$. Positive current indicates charge and negative current indicates discharge.

Definition 3: K cells in the training set are denoted by indices $1, \ldots, K$. Therefore, the C/20 charge capacity trajectories in the training set are $Q^1, \ldots, Q^K$, denoted by Q^{train}. The aging-cycle charge throughput trajectories in the training set are $Q_{\mathrm{age}}^1, \ldots, Q_{\mathrm{age}}^K$, denoted by $Q_{\mathrm{age}}^{\mathrm{train}}$. Other than the aging-cycle charge throughput trajectories, there are many other feature trajectories in the training set. We denote all the feature trajectories in the training set by $X_{\mathrm{age}}^{\mathrm{train}}$.

Definition 4: The one cell in the test set is denoted by index z. Therefore, the C/20 charge capacity trajectory in the test set is Q^z, denoted by Q^{test}. The aging-cycle charge throughput trajectory in the test set is Q_{age}^z, denoted by $Q_{\mathrm{age}}^{\mathrm{test}}$. Other than the aging-cycle charge throughput trajectories, there are many other feature trajectories in the test set. We denote all the feature trajectories in the test set by $X_{\mathrm{age}}^{\mathrm{test}}$.

Definition 5: The adaptive battery health estimator $\mathcal{E}_H$ is a type of data-driven estimator of the form

$$\hat{Q}^{\mathrm{test}} = f\left(X_{\mathrm{age}}^{\mathrm{test}}, X_{\mathrm{age}}^{\mathrm{train}}, Q^{\mathrm{train}}\right) \tag{10}$$

where f is a generic mapping function, $\hat{Q}^{\mathrm{test}}$ represents the estimated C/20 charge capacity of the cell in the test set, Q^{train} and $X_{\mathrm{age}}^{\mathrm{train}}$ are defined in Definition 3, and $X_{\mathrm{age}}^{\mathrm{test}}$ is defined in Definition 4.

The estimation error e_n is evaluated as

$$e = \hat{Q}^{\mathrm{test}} - Q^{\mathrm{test}} \tag{11}$$

where Q^{test} is defined in Definition 4.

Stability is of practical importance for adaptive estimation laws as it ensures that the proposed estimation process does not result in divergence. This article uses the notion of bounded-input, bounded-output stability defined as follows.

Definition 6: An adaptive battery health estimator $\mathcal{E}_H$ defined in Definition 5 is BIBO stable if for any bounded input signal with $\|X_{\mathrm{age}}^{\mathrm{train}}\| < \infty$, $\|X_{\mathrm{age}}^{\mathrm{test}}\| < \infty$, $\|Q^{\mathrm{train}}\| < \infty$, $\|Q^{\mathrm{test}}\| < \infty$, the error e_n satisfies $\|e_n\| < \infty$.

Remark 5: BIBO stability ensures that any bounded input variations, such as fluctuations in online features, lead only to bounded variations in SOH estimation. This prevents prediction divergence, even under changing operating conditions or transient inputs.

A. Clustering-Based Adaptive Estimation

The clustering-based adaptive estimation algorithm aims to find the trajectory in the training set that is closest to the trajectory in the test set. The closeness metric is defined by the following distance function:

Definition 7: The distance between two aging-cycle charge throughput trajectories Q_{age}^x and Q_{age}^y is defined as

$$\mathrm{dist}\left(Q_{\mathrm{age}}^x, Q_{\mathrm{age}}^y\right) = \sqrt{\sum_{i=1}^{n}\left(Q_{\mathrm{age}}^x(\mathrm{Ah}_i) - Q_{\mathrm{age}}^y(\mathrm{Ah}_i)\right)^2} \quad 1 \le n \le N. \tag{12}$$

Remark 6: The pseudocode to calculate the distance can be found in Algorithm 1. $\mathrm{dist}(Q_{\mathrm{age}}^x, Q_{\mathrm{age}}^y)$ is a nonnegative and a symmetric quantity.

Compared with the nearest-neighbor distance metric based on the latest measurements, this trajectory distance metric accounts for the complete historical differences between Q_{age}^x and Q_{age}^y and evaluates similarities based not only on instantaneous measurements but also on historical capacity measurements. Therefore, this distance metric allows more robust classification in the presence of one-shot measurement noise. One shortcoming of this distance metric is that it requires more than one data point to make a definitive classification. However, in the long run, when the online BMS$_2$ has accumulated enough information, the additional data requirement can be easily met. This distance function can be easily generalized to measure the distance between other trajectories such as the C/20 charge capacity trajectory.

Each time a new sample from cell z is collected, the classification is updated to assign cell z to a cluster index.

Definition 8: Classification index sequence for cell z, $\{S_n^z\} = (S_1^z, S_2^z, \ldots, S_N^z)$, is a discrete-time sequence defined by

$$S_n^z = \underset{1\le k\le K}{\mathrm{argmin}}\ \mathrm{dist}\left(Q_{\mathrm{age}}^z\left(\{\mathrm{Ah}_i\}_{i\le n}\right), Q_{\mathrm{age}}^k\left(\{\mathrm{Ah}_i\}_{i\le n}\right)\right) \tag{13}$$

where $n \in [1, 2, \ldots, N]$, Q_{age}^z and Q_{age}^k are the aging-cycle charge trajectories of cells z and k, respectively. The distance function dist has been defined in Definition 7. An example

Algorithm 1 Calculate Distance

function CALCULATEDISTANCE($Q^x_{\text{age}}(Ah_1, \cdots, Ah_N)$, $Q^y_{\text{age}}(Ah_1, \cdots, Ah_N)$)
  distance $\leftarrow 0$ ▷ Initialize distance to zero
  for i from 1 to n **do**
    diff $\leftarrow Q^x_{\text{age}}(Ah_i) - Q^y_{\text{age}}(Ah_i)$
    distance $\leftarrow$ distance + diff^2
  end for
  distance $\leftarrow \sqrt{\text{distance}}$ ▷ Calculate the square root
  return distance ▷ Return the distance
end function

Algorithm 2 Classification Index Sequence

function CLASSIFICATIONINDEXSEQUENCE($Q^z_{\text{age}}(Ah_1, \cdots, Ah_N)$, $Q^1_{\text{age}}(Ah_1, \cdots, Ah_N)$, $\cdots$, $Q^K_{\text{age}}(Ah_1, \cdots, Ah_N)$)
  Initialize an empty sequence S^z
  for n from 1 to N **do**
    minDist $\leftarrow \infty$ ▷ Initialize minimum distance to positive infinity
    $S^z_n \leftarrow 0$ ▷ Initialize the classification index for the current time step
    for k from 1 to K **do**
      dist $\leftarrow$ CALCULATEDISTANCE($Q^z_{\text{age}}(Ah_1, Ah_2, \cdots, Ah_n)$, $Q^k_{\text{age}}(Ah_1, Ah_2, \cdots, Ah_n)$)
      if dist $<$ minDist **then**
        minDist $\leftarrow$ dist ▷ Update minimum distance
        $S^z_n \leftarrow k$ ▷ Update the classification index
      end if
    end for
    Append S^z_n to S^z ▷ Add the classification index to the sequence
  end for
  return S^z ▷ Return the classification index sequence
end function

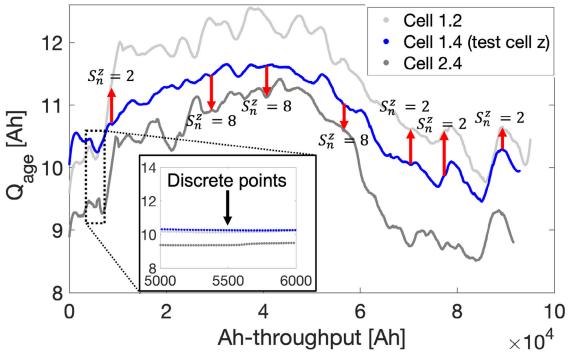

Fig. 5. Example of cell classification defined in Definition 8 with Cell 1.4 as the test cell compared against Cell 1.2 ($S^z_n = 2$) and Cell 2.4 ($S^z_n = 8$). Red arrows point to the aging-cycle charge trajectory with the minimum distance from Q^z_{age}—where $z = 1.4$—at different Ah-throughputs. The zoomed plot shows that these are highly dense discrete points since Q^z_{age} is extracted from every cycle.

of cell classification is shown in Fig. 5. The pseudocode to calculate the classification index sequence can be found in Algorithm 2.

Theorem 1: Consider a data-driven estimator described in Definition 5. Let the battery cells $1, \ldots, K$ be the training set and cell z be the test set. If the model parameters λ_k are adapted according to

$$\lambda_k = \frac{\sum_{n=1}^{N} \chi\left(S^z_n = k\right) \text{Ah}_n}{\sum_{n=1}^{N} \text{Ah}_n} \tag{14}$$

where

$$\chi\left(S^z_n = k\right) = \begin{cases} 1, & \text{if } S^z_n = k, \quad 1 \le k \le K \\ 0, & \text{otherwise} \end{cases} \tag{15}$$

and S^z_n is defined in (13). Then the clustering-based health estimator, formulated as

$$\hat{Q}^{ct}(\text{Ah}_n) = Q^z_0 \hat{\bar{Q}}^{ct}(\text{Ah}_n) \tag{16}$$

$$\hat{\bar{Q}}^{ct}(\text{Ah}_n) = \sum_{k=1}^{K} \lambda_k \bar{Q}^k(\text{Ah}_n) \tag{17}$$

where $\hat{Q}^{ct}$, the estimation target, represents the estimated C/20 charge capacity of cell z, is BIBO stable.

Remark 7: The pseudocode for the clustering-based adaptive estimation can be found in Algorithm 3. The tuning parameters λ_k can be thought of as forgetting factors, assigning greater weight to the most recent classification result while retaining the memory of past classification outcomes to enhance robustness.

Proof: From (14), λ_k is designed to be positive. Moreover, λ_k satisfies

$$\sum_{k=1}^{K} \lambda_k = 1. \tag{18}$$

Algorithm 3 Clustering-Based Adaptive Estimator

Require:

N: Trajectory length or the number of data points on a trajectory

K: Number of cells in the training set

S_n^z: Array representing the classification index sequence

Ah_n: Array representing the accumulated Ah throughput

Q_0^z: Initial SOH of cell z

Initialize an array for lambda values with size K: $\lambda = [0] * K$

Initialize an array for $\bar{Q}^z$ values with size N: $\bar{Q}^z = [0] * N$

Ensure:

Calculate the denominator for lambda:

denominator $= 0$

for $n = 1$ to N **do**

denominator$+ = Ah_n[n]$

end for

Calculate lambda values for each training cell:

for $k = 1$ to K **do**

numerator $= 0$

for $n = 1$ to N **do**

if $S_n^z[n] = k$ **then**

numerator$+ = Ah_n[n]$

end if

end for

$\lambda[k]$ = numerator/denominator

end for

Calculate $\bar{Q}^z$ for the cell in the test set:

for $n = 1$ to N **do**

$\bar{Q}^z[n] = 0$

for $k = 1$ to K **do**

$\bar{Q}^z[n]+ = \lambda[k] \cdot \bar{Q}^k(Ah_n[n])$

end for

end for

Calculate Q^z:

for $n = 1$ to N **do**

$Q^z[n] = Q_0^z \cdot \bar{Q}^z[n]$

end for

The estimated SOH of the cell in the test set is stored in the array Q^z

This can be proved by

$$\sum_{k=1}^{K} \lambda_k = \sum_{k=1}^{K} \frac{\sum_{n=1}^{N} \chi\left(S_n^z = k\right) \mathrm{Ah}_n}{\sum_{n=1}^{N} \mathrm{Ah}_n} \tag{19}$$

$$= \sum_{n=1}^{N} \frac{\sum_{k=1}^{K} \chi\left(S_n^z = k\right) \mathrm{Ah}_n}{\sum_{n=1}^{N} \mathrm{Ah}_n} \tag{20}$$

$$= \sum_{n=1}^{N} \frac{\mathrm{Ah}_n}{\sum_{n=1}^{N} \mathrm{Ah}_n} = 1. \tag{21}$$

To prove the BIBO stability, from Definition 6, the K SOH trajectories $\{Q_n^1\}, \ldots, \{Q_n^K\}$ in the training set are bounded

$$\|Q^k\| < \infty, \quad \text{for } 1 \le k \le K. \tag{22}$$

From Definition 6, the SOH trajectory $\{Q_n^z\}$ in the test set is bounded

$$\|Q^z\| < \infty. \tag{23}$$

The error trajectory between the estimated capacity and the true capacity follows

$$\left\|\hat{Q}^{ct} - Q^z\right\| \overset{(16)}{=} \left\|Q_0^z \hat{\bar{Q}}^{ct} - Q^z\right\| \tag{24}$$

$$\overset{(17)}{=} \left\|Q_0^z \sum_{k=1}^{K} \lambda_k \bar{Q}^k - Q^z\right\| \tag{25}$$

$$\overset{(18)}{=} \left\|Q_0^z \sum_{k=1}^{K} \lambda_k \bar{Q}^k - \sum_{k=1}^{K} \lambda_k Q^z\right\| \tag{26}$$

$$\overset{(9)}{=} \left\|Q_0^z \sum_{k=1}^{K} \lambda_k \bar{Q}^k - Q_0^z \sum_{k=1}^{K} \lambda_k \bar{Q}^z\right\| \tag{27}$$

$$= Q_0^z \left\| \sum_{k=1}^{K} \lambda_k \left(\bar{Q}^k - \bar{Q}^z\right) \right\|. \tag{28}$$

From (18) and (28)

$$\left\|\hat{Q}^{ct} - Q^z\right\| \le Q_0^z \max_{1 \le k \le K} \{\left\|\bar{Q}^k - \bar{Q}^z\right\|\} \tag{29}$$

$$\le \max_{1 \le k \le K} \{\left\|Q^k\right\|\} + \|Q^z\| < \infty. \tag{30}$$

Therefore, the error trajectory is bounded. From Definition 6, the BIBO stability is guaranteed. □

This proof aims to demonstrate that the estimation error of the test cell's SOH is bounded by a function of the SOH values of all the cells in the training set. The adaptive clustering-based approach in BMS$_2$ addresses the distance metric issue by progressively refining the clusters as more data are collected. As the system accumulates operational data, it continuously recalculates the distance metric using a weighted historical average of prior measurements, which reduces the impact of outliers and transient behaviors. This approach ensures that the distance metric stabilizes and accurately reflects the battery's unique degradation pattern over time.

B. Adaptive Estimation by Combining the Clustering and Regression

The clustering-based method proposed in this study can exhibit a significant classification error when there is limited observation available for the cell under test. To address this limitation, we combine the clustering-based estimation and the regression-based estimation. In this article, we use the offline ENR model, a specific regression-based estimator, as introduced in Section IV.

Theorem 2: Consider the data-driven estimator described in Definition 5. The adaptive unitless weight parameters $w_1, w_2 \in \mathbb{R}^+$ follows

$$w_2 = \begin{cases} \alpha \mathrm{Ah}, & \text{if } \alpha \mathrm{Ah} < 0.5 \\ 0.5, & \text{otherwise} \end{cases} \tag{31}$$

$$w_1 = 1 - w_2 \tag{32}$$

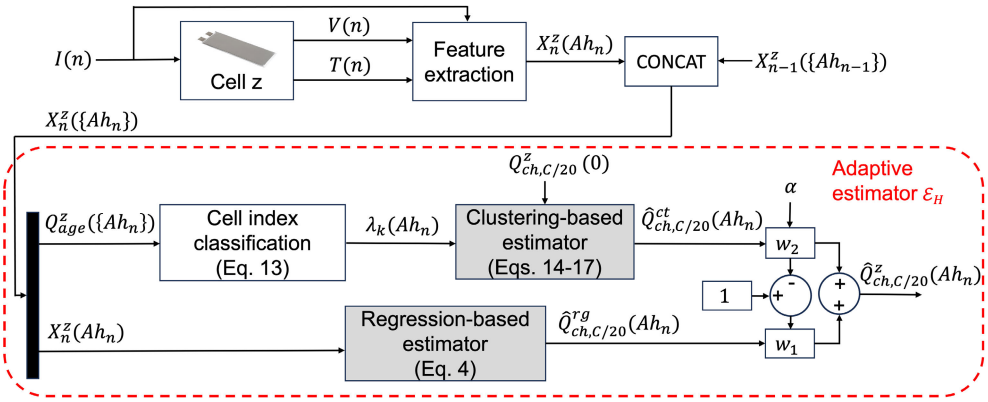

Fig. 6. Block diagram showing current $I(n)$, voltage $V(n)$, and cell surface temperature $T(n)$ used to extract features at time n. The extracted features are concatenated with features at time instant $n-1$ and this complete sequence of features is input to the adaptive estimator. Output $\hat{Q}^z_{\text{ch,C/20}}$ is obtained through a weighted sum of the output from clustering-based estimator and regression-based estimator (offline ENR model). Clustering-based estimator uses only the complete sequence of Ah-throughput $\{\text{Ah}_n\}$ and aging-cycle charge trajectory $Q^z_{\text{age}}(\{\text{Ah}_n\})$ that is observed while all the signals from X^z_n at the current time instance are used for the regression-based estimation.

where α is a fixed constant, in the unit of Ah^{-1}. Then the adaptive estimator, formulated as

$$\hat{Q}^z(\text{Ah}_n) = w_1\hat{Q}^{rg}(\text{Ah}_n) + w_2\hat{Q}^{ct}(\text{Ah}_n) \tag{33}$$

is BIBO stable.

Remark 8: The adaptive estimation is obtained by summing the two estimation results with weights assigned to them. The weight parameters w_1 and w_2 allocate increasing importance to the online model as time progresses, while still preserving the influence of the offline model. Specifically, w_1 starts higher during the early stages of the estimation process because, at this stage, the regression model has access to the historical training data, which offers a more reliable SOH estimation. As more operational data become available, w_2 increases because the clustering-based method can start accurately grouping the test battery with similar batteries in the training set. This tradeoff between w_1 and w_2 can be realized by α.

Remark 9: α can be interpreted as a learning-rate constant, measured in units of Ah^{-1}, with a range of values from 0 to $+\infty$. It is recommended to initially set α to $\alpha = 1/20$ $\text{Ah}_{\max}$ at the outset, where $\text{Ah}_{\max}$ represents the largest Ah throughputs that the batteries are expected to be cycled during its SL. Subsequently, α can be adjusted using the data in the training set. For example, the designer can gradually increase α until the point at which the validation error begins to rise. Sensitivity analysis of α for Cells 1.2, 1.4, and 2.3 is shown in Section V-B1.

Proof: The error trajectory between the estimated capacity and the true capacity follows

$$\|\hat{Q}^z - Q^z\| \tag{34}$$

$$\overset{(33)}{=} \left\| \left(w_1\hat{Q}^{rg} + w_2\hat{Q}^{rg}\right) - (w_1+w_2)Q^z) \right\| \tag{35}$$

$$= \left\|w_1(\hat{Q}^{rg} - Q^z) + w_2(\hat{Q}^{ct} - Q^z)\right\| \tag{36}$$

$$\leq w_1\left\|\hat{Q}^{rg} - Q^z\right\| + w_2\left\|\hat{Q}^{ct} - Q^z\right\|. \tag{37}$$

From Theorem 1, the second term $w_2\|\hat{Q}^{ct} - Q^z\|$ in (37) is bounded. To prove the stability, from Definition 6, the feature trajectories in the training set are bounded

$$\left\|X^{\text{train}}_{\text{age}}\right\| < \infty. \tag{38}$$

From (38) and (23), the first term in (37) is bounded by

$$\left\|\hat{Q}^{rg} - Q^z\right\| \tag{39}$$

$$= \left\|X^{\text{train}}_{\text{age}}\beta + \beta_0 - Q^z\right\| \tag{40}$$

$$\leq \left\|X^{\text{train}}_{\text{age}}\right\| \|\beta\| + \|\beta_0\| + \|Q^z\| < \infty. \tag{41}$$

Therefore, the error trajectory is bounded and the BIBO stability is guaranteed. □

By combining (30) and (41), we confirm that the adaption error remains bounded and does not diverge to infinity. This result satisfies the criteria for BIBO stability in Definition 6, meaning that any bounded fluctuations in online features lead only to bounded variations in SOH estimation. The complete flow of information for the adaptive estimator is shown in Fig. 6. In summary, the adaptive law used in the estimation process does not cause the estimation to diverge, and the worst case error in health estimation can be bounded. The size of the error ball is determined by the errors of the offline model and adaptive model. Furthermore, the radius of the error ball can be further reduced by tuning the gains w and λ.

1) Sensitivity Analysis of Learning-Rate Constant α: For the adaptive estimator given in Section V-B, α is used to adapt w_2 to control the contribution of $\hat{Q}^{ct}(\text{Ah}_n)$ in the output. The range is given by $\alpha = [0, +\infty)$, which means it is important to choose a suitable value of α to ensure the best performance from the estimator. In this sensitivity analysis, three different ranges of α values are tested, and each range consists of five linearly spaced points, including the boundary values. These ranges are given by: 1) range $r_1 = [0, 5 \times 10^{-6}]$; 2) range $r_2 = [6 \times 10^{-6}, 1]$; and 3) range $r_3 = [11, 100]$ as shown in Fig. 7.

For sensitivity analysis, the RMSE is observed for different α values and the results are compared with the current α value used in our results. Fig. 8 shows the sensitivity of α for Cell 1.2. It can be seen that α_{current}—the current value

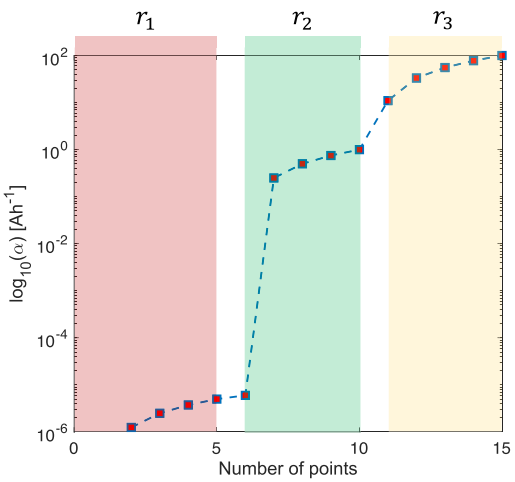

Fig. 7. Range of α values used for sensitivity analysis shown on a log-scale. Three distinct ranges r_1, r_2, and r_3 are considered that contain linearly spaced points at different α values. Note: Due to the use of log-scale, $\alpha = 0$ is not visible in r_1.

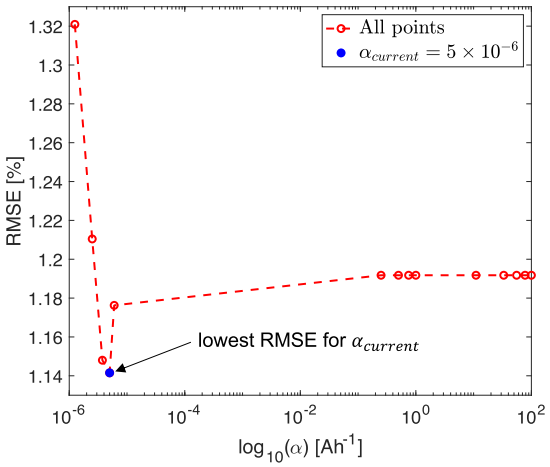

Fig. 8. Sensitivity analysis of α for Cell 1.2. $\alpha_{\text{current}} = 5 \times 10^{-6}$ has the lowest RMSE among all α values.

of α—gives the lowest RMSE for the entire range of values. In fact, using values smaller or greater than α_{current} increases the RMSE value. Repeating the same analysis for Cell 1.4 as shown in Fig. 9, we can see that α_{current} does not give the smallest RMSE; instead, the smallest RMSE is obtained at $\alpha = 6 \times 10^{-6}$. An extra set of linearly spaced 10 points between $[6 \times 10^{-6}, 0.25]$ is analyzed and it can be seen that lowest RMSE is still obtained at the same value. It should be noted that $\alpha = 5 \times 10^{-6}$ is a close second in terms of lowest RMSE with a difference of less than 0.1% for the lowest RMSE value.

Finally, for Cell 2.3, the sensitivity analysis results are shown in Fig. 10. It can be seen that neither $\alpha = 5 \times 10^{-6}$ nor $\alpha = 6 \times 10^{-6}$ give the lowest RMSE value. Instead, by analyzing 18 further points between $[6 \times 10^{-6}, 0.25]$, it can be seen that the lowest RMSE is obtained for a range of values at $\alpha \geq 2.8 \times 10^{-4}$. One thing to note here is that Cell 2.3 has the largest errors in the offline ENR model which means relativity larger contribution of the clustering-based estimator $\hat{Q}^{ct}(\text{Ah}_n)$ is needed to improve the estimation of the model.

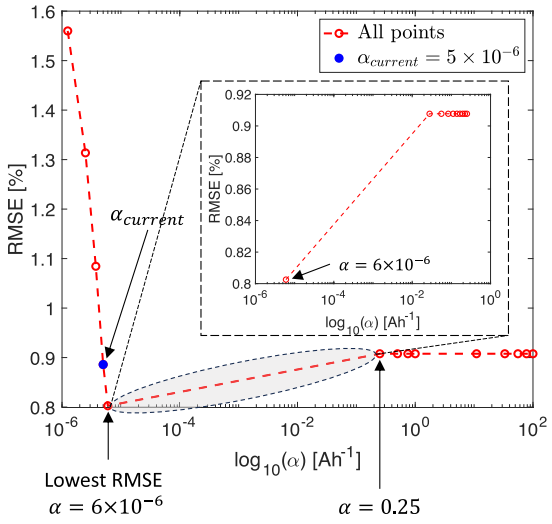

Fig. 9. Sensitivity analysis of α for Cell 1.4. $\alpha = 6 \times 10^{-6}$, which is greater than α_{current}, has the lowest RMSE value. Between $\alpha = 6 \times 10^{-6}$ and $\alpha = 0.25$, ten extra values of α are analyzed; however, the lowest RMSE is still obtained at $\alpha = 6 \times 10^{-6}$.

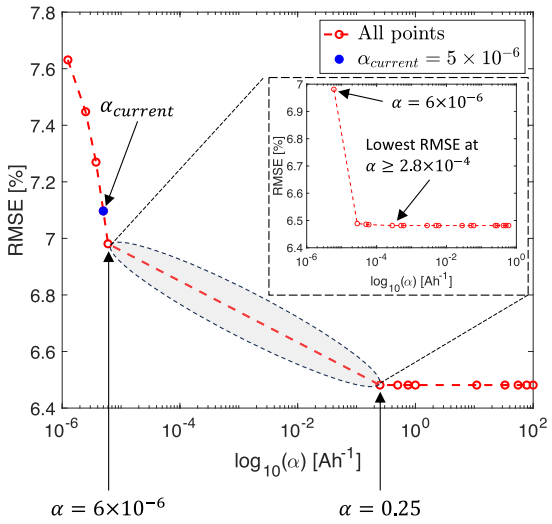

Fig. 10. Sensitivity analysis of α for Cell 2.3. $\alpha \geq 0.25$ has lower RMSE than α_{current}. Between $\alpha = 6 \times 10^{-6}$ and $\alpha = 0.25$ 18 extra values of α are analyzed, and it is observed that the lowest RMSE value is obtained for $\alpha \geq 2.8 \times 10^{-4}$.

VI. Results and Discussion

The performance of the proposed online adaptive estimation algorithm is demonstrated in several case studies. In the first demonstration, we leave out Cell 1.4 for testing and train the model using the remaining seven cells. The C/20 charge capacity trajectories estimated by the ENR model and online adaptive model are illustrated in Fig. 11(a) and (b), respectively.

Initially, when the Ah-throughput is lower, the weight w_1 is large, while the weight w_2 is small. The ENR-based estimate dominates the overall estimate. Therefore, the ENR model and adaptive model coincide at the same starting point, as demonstrated in Fig. 11(a). As Ah-throughput increases to Ah $> 2 \times 10^4$ Ah, the classification index converges to the nearest cluster (cluster 8/Cell 2.4), as depicted in Fig. 11(c). However, it is observed that after Ah-throughput increases to Ah $> 6.5 \times 10^4$ Ah, the classification index

TABLE II
LEAVE-ONE-OUT TESTS OF TWO HEALTH ESTIMATION METHODS

RMSPE [%]	Cell 1.1	Cell 1.2	Cell 1.3	Cell 1.4	Cell 2.1	Cell 2.2	Cell 2.3	Cell 2.4
Adaptive Estimation	2.93	1.22	2.62	0.86	2.26	3.82	7.27	0.95
ENR-based Estimation	2.95	1.47	2.41	1.82	1.45	3.27	7.82	1.58

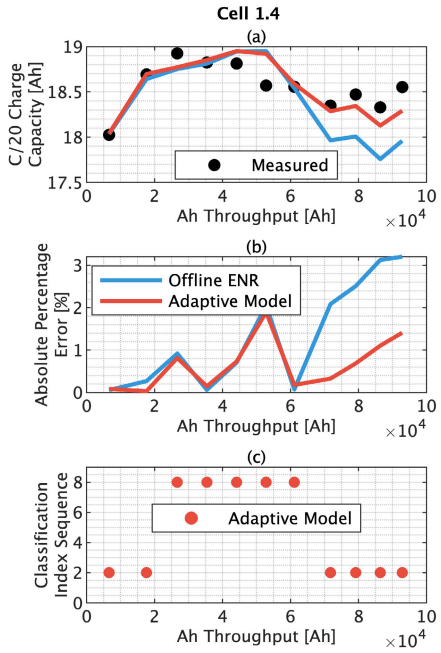

Fig. 11. Performance evaluation of the online adaptive estimator for Cell 1.4. (a) C/20 charge capacity trajectories estimated from the offline ENR and online adaptive model are compared against the measured capacity. (b) Pointwise absolute capacity estimation percentage error of the offline ENR is compared against that of the online adaptive model. RMSE of the online adaptive model is 0.8610%. (c) Classification index sequence, as defined in Definition 8, of the online adaptive estimator.

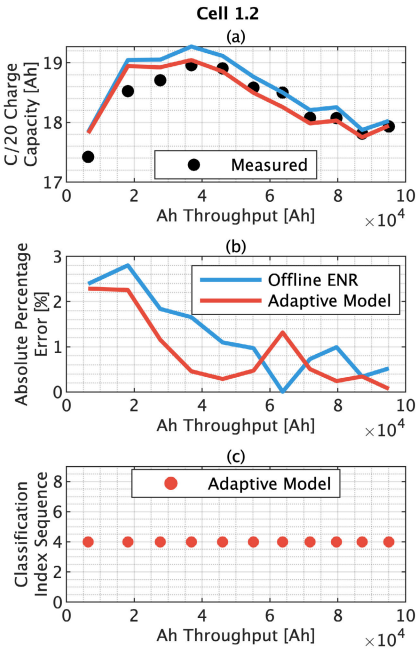

Fig. 12. Performance evaluation of the online adaptive estimator for Cell 1.2. (a) C/20 charge capacity trajectories estimated from the offline ENR and online adaptive model are compared against the measured capacity. (b) Pointwise absolute capacity estimation percentage error of the offline ENR is compared against that of the online adaptive model. The RMSE of the online adaptive model is 1.2182%. (c) Classification index sequence, as defined in Definition 8, of the online adaptive estimator.

is again perturbed to the wrong cluster (cluster 2/Cell 1.2). Due to the weight adaptation law (14), the overall estimation output is only slightly impacted by the wrong classification. Early in the aging campaign, ENR estimation dominates the overall prediction, so changes in the classification index—and consequently in clustering-based estimation—have a limited impact on SOH estimation. However, as aging progresses, the clustering-based component gains influence, providing more accurate adjustments to the SOH. This is why, in the latter half of the aging cycle, as shown in Fig. 11, the adaptive estimation using clustering-based methods becomes more prominent and eventually surpasses ENR.

Because the adaptive SOH estimator continuously processes the real-time influx of data, it yields reduced estimation errors. As displayed in Fig. 11(b), using solely the ENR model yields a maximum absolute pointwise percentage error of 3%, and a root-mean-squared pointwise percentage error of 1.8166%. In contrast, by leveraging the online adaptive model that combines the ENR-based estimation and clustering-based estimation, the maximum pointwise percentage error decreases to 2%, and the root-mean-squared pointwise percentage error decreases to 0.8610%.

Weight adaptation avoids the hazards that the online clustering-based model causes by underinformed classification in the beginning when little data are collected. Weight λ balances the contributions of the current-step classification result and historical-step classification results. These historical-step classification results are memorized by summing their corresponding Ah-throughput. This effectively decreases the high sensitivity of the online clustering-based estimation method to the current-step classification result.

The adaptive model's classification index can sometimes shift due to transient changes in the battery's internal state, such as temporary variations in environmental factors such as temperature fluctuations. These short-term variations may cause the algorithm to momentarily assign an incorrect cluster, particularly at specific Ah-throughput levels where degradation patterns exhibit subtle changes. However, the adaptive nature of the model allows it to recalibrate as more data are collected and correct these misclassifications over time to preserve the overall model stability. From a practical perspective, while these temporary misclassifications may introduce slight deviations in SOH estimation, the model's BIBO stability ensures that they do not significantly affect long-term accuracy.

In another demonstration, as shown in Fig. 12, the online adaptive estimation algorithm was tested on Cell 1.2, where the ENR had already demonstrated good performance. Incorporating the online adaptive estimator further reduced the pointwise

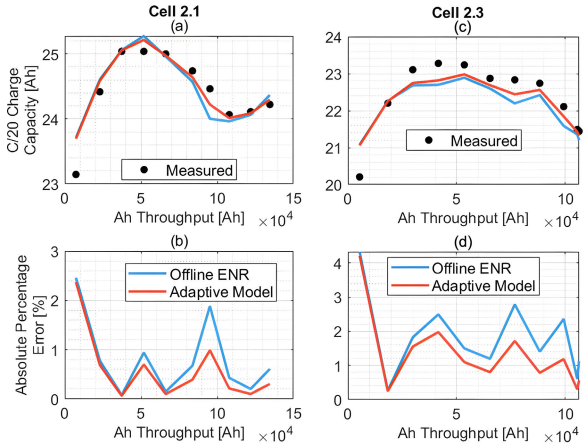

Fig. 13. Performance comparison between the online adaptive estimator and the offline ENR estimator. The C/20 charge capacity trajectory estimations for Cell 2.1 and Cell 2.3 are shown in (a) and (c), respectively. The pointwise absolute percentage errors in capacity estimation for Cell 2.1 and Cell 2.3 are illustrated in (b) and (d), respectively.

percentage RMSE of capacity estimation from 1.4686% to 1.2182%.

Moreover, the adaptive estimation algorithm has been tested on the remaining six cells. In each test, we perform a leave-one-out test on the entire dataset, leaving only the cell under test in the test set and including the rest of the seven cells in the training set. The averaged RMSPE over eight test cases of the ENR-based estimation is 3.40%, while the RMSPE over eight test cases of the adaptive estimation is 3.27%. The RMSPE for each training–testing set split is presented in Table II.

For Cells 2.1 and 2.3, an additional year of new data (from April 2023 to April 2024) was used to assess the algorithm's generalizability. The training set consisted of the original data from six other cells (collected from January 2022 to April 2023). As illustrated in Fig. 13, the absolute percentage error at the end of the experiment remains below 0.5% for Cells 2.1 and 2.3, demonstrating the robustness and generalizability of the proposed algorithm.

In addition to accuracy, the computational efficiency of the adaptive estimation model is critical for large-scale BMS that requires real-time processing. The adaptive SOH estimator is designed to operate efficiently on standard embedded processors commonly used in BMS. The computational requirements primarily involve matrix operations for ENR and iterative clustering algorithms for the adaptive component. On a modern embedded processor, these operations can be executed within milliseconds, ensuring real-time adaptability without significant processing overhead. Memory usage is minimized by storing only the most recent clusters and model parameters, enabling the estimator to run continuously without substantial hardware upgrades.

The adaptive SOH estimator can be modularly embedded in existing BMS software architectures. The estimator requires real-time data inputs, such as voltage, current, temperature, and cumulative charge/discharge cycles, which are already monitored by conventional BMS. This flexibility makes the estimator a suitable retrofit option for the existing BMS frameworks, enhancing their capability for SL applications without substantial redesign. In addition, the lightweight computational footprint of the estimator ensures it can scale across a range of battery configurations and capacities typical of SL deployments.

VII. Conclusion

Due to its high flexibility and model agnosticism, data-driven health estimation has emerged as a valid and viable method for assessing the health of SL batteries. To enable the in-the-field operation of SL battery energy storage systems, we present an online adaptive data-driven health estimation method with guaranteed BIBO stability. The clustering-based estimation is combined together with the ENR. We have validated this method using a dataset of laboratory-aged SL batteries retired from commercial EVs. Our method gives good performance on different test cells and also shows improvement in RMSE for certain test cases.

Further work can focus on enhancing the robustness of this method. One limitation is its reliance on operational data, which can introduce variability in estimation accuracy due to differences in battery operating conditions that the model may not fully capture. To address this, future research could explore integrating additional real-time sensors to capture more detailed operational metrics, such as stress and strain, thereby improving the accuracy of the estimations. Alternatively, acknowledging the inevitable errors in SOH estimation, another promising direction is to design power electronics with built-in redundancy. This approach would enable the system to compensate for the uncertainties arising from the SOH inaccuracies of heterogeneous SL batteries [48], [49].

Acknowledgment

Special thanks to Gabriele Pozzato and Nhat Nguyen for their technical discussions and data processing efforts. The authors would also like to thank Gabriele Marini for proof-reading and commenting on this article.

References

[1] N. Lutsey, M. Grant, S. Wappelhorst, and H. Zhou, "Power play: How governments are spurring the electric vehicle industry," in *Proc. ICCT*, Washington, DC, USA, 2018, pp. 1–41.

[2] J. Eddy, A. Pfeiffer, and J. van de Staaij, *Recharging Economies: The EV-Battery Manufacturing Outlook for Europe*. New York, NY, USA: McKinsey & Company, 2019.

[3] W. Li, Z. Bao, Q. Gao, Q. Du, and K. Jiao, "Investigation of novel pulse preheating strategies for lithium-ion batteries at subzero temperature based on a multi-level CFD platform," *eTransportation*, vol. 19, Jan. 2024, Art. no. 100307.

[4] W. Li, Q. Du, G. Guo, C. Wu, and K. Jiao, "Enhanced electrochemical and thermal behavior of lithium-ion batteries with ultrathick electrodes via oriented pores," *Appl. Thermal Eng.*, vol. 228, Jun. 2023, Art. no. 120555.

[5] N. Brinkel, L. Visser, W. van Sark, and T. AlSkaif, "A novel forecasting approach to schedule aggregated electric vehicle charging," *Energy AI*, vol. 14, Oct. 2023, Art. no. 100297.

[6] P. Pavlínek, "Transition of the automotive industry towards electric vehicle production in the east European integrated periphery," *Empirica*, vol. 50, no. 1, pp. 35–73, Feb. 2023.

[7] B. Jones, V. Nguyen-Tien, and R. J. R. Elliott, "The electric vehicle revolution: Critical material supply chains, trade and development," *World Economy*, vol. 46, no. 1, pp. 2–26, Jan. 2023.

[8] Q. Dong, S. Liang, J. Li, H. C. Kim, W. Shen, and T. J. Wallington, "Cost, energy, and carbon footprint benefits of second-life electric vehicle battery use," *iScience*, vol. 26, no. 7, Jul. 2023, Art. no. 107195.

[9] X. Gu et al., "Challenges and opportunities for second-life batteries: Key technologies and economy," *Renew. Sustain. Energy Rev.*, vol. 192, Mar. 2024, Art. no. 114191.

[10] Z. Song, M. S. Nazir, X. Cui, I. A. Hiskens, and H. Hofmann, "Benefit assessment of second-life electric vehicle lithium-ion batteries in distributed power grid applications," *J. Energy Storage*, vol. 56, Nov. 2022, Art. no. 105939.

[11] K. Moy and S. Onori, "Synthetic grid storage duty cycles for second-life lithium-ion battery experiments," *SAE Int. J. Adv. Current Practices Mobility*, vol. 6, pp. 261–269, Jan. 2023.

[12] S. Vignesh et al., "State of health (SoH) estimation methods for second life lithium-ion battery—Review and challenges," *Appl. Energy*, vol. 369, May 2024, Art. no. 123542. [Online]. Available: https://www.sciencedirect.com/science/article/pii/S0306261924009255

[13] X. Cui, M. Aadil Khan, S. Singh, R. Sharma, and S. Onori, "Adaptive health monitoring of second-life batteries," in *Proc. Amer. Control Conf. (ACC)*, Jul. 2024, pp. 1–6. doi: 10.23919/ACC60939.2024.10644309.

[14] E. Martinez-Laserna et al., "Evaluation of lithium-ion battery second life performance and degradation," in *Proc. IEEE Energy Convers. Congr. Expo. (ECCE)*, Sep. 2016, pp. 1–7.

[15] A. Weng, E. J. Dufek, and A. G. Stefanopoulou, "Battery passports for promoting electric vehicle resale and repurposing," *Joule*, vol. 7, no. 5, pp. 837–842, Apr. 2023.

[16] L. Serrao, S. Onori, G. Rizzoni, and Y. Guezennec, "A novel model-based algorithm for battery prognosis," *IFAC Proc. Volumes*, vol. 42, no. 8, pp. 923–928, Jan. 2009.

[17] F. Todeschini, S. Onori, and G. Rizzoni, "An experimentally validated capacity degradation model for Li-ion batteries in PHEVs applications," *IFAC Proc. Volumes*, vol. 45, no. 20, pp. 456–461, Jan. 2012.

[18] N. Yang et al., "An improved semi-empirical model for thermal analysis of lithium-ion batteries," *Electrochim. Acta*, vol. 311, pp. 8–20, Apr. 2019.

[19] M. Varini, P. E. Campana, and G. Lindbergh, "A semi-empirical, electrochemistry-based model for Li-ion battery performance prediction over lifetime," *J. Energy Storage*, vol. 25, Oct. 2019, Art. no. 100819.

[20] G. Pozzato, S. B. Lee, and S. Onori, "Modeling degradation of lithium-ion batteries for second-life applications: Preliminary results," in *Proc. IEEE Conf. Control Technol. Appl. (CCTA)*, Aug. 2021, pp. 826–831.

[21] R. Fu, S.-Y. Choe, V. Agubra, and J. Fergus, "Development of a physics-based degradation model for lithium ion polymer batteries considering side reactions," *J. Power Sources*, vol. 278, pp. 506–521, Mar. 2015.

[22] A. Jana, A. S. Mitra, S. Das, W. C. Chueh, M. Z. Bazant, and R. E. García, "Physics-based, reduced order degradation model of lithium-ion batteries," *J. Power Sources*, vol. 545, Oct. 2022, Art. no. 231900.

[23] G. Dong and J. Wei, "A physics-based aging model for lithium-ion battery with coupled chemical/mechanical degradation mechanisms," *Electrochim. Acta*, vol. 395, Nov. 2021, Art. no. 139133.

[24] X. Hu et al., "A review of second-life lithium-ion batteries for stationary energy storage applications," *Proc. IEEE*, vol. 110, no. 6, pp. 735–753, Jun. 2022.

[25] M. Mitici, B. Hennink, M. Pavel, and J. Dong, "Prognostics for lithium-ion batteries for electric vertical take-off and landing aircraft using data-driven machine learning," *Energy AI*, vol. 12, Apr. 2023, Art. no. 100233.

[26] H.-A.-I. El-Azab, R. A. Swief, N. H. El-Amary, and H. K. Temraz, "Seasonal electric vehicle forecasting model based on machine learning and deep learning techniques," *Energy AI*, vol. 14, Oct. 2023, Art. no. 100285.

[27] Y. Jiang, J. Jiang, C. Zhang, W. Zhang, Y. Gao, and N. Li, "State of health estimation of second-life $LiFePO_4$ batteries for energy storage applications," *J. Cleaner Prod.*, vol. 205, pp. 754–762, Sep. 2018. [Online]. Available: https://www.sciencedirect.com/science/article/pii/S0959652618328725

[28] J. Wei, G. Dong, and Z. Chen, "Remaining useful life prediction and state of health diagnosis for lithium-ion batteries using particle filter and support vector regression," *IEEE Trans. Ind. Electron.*, vol. 65, no. 7, pp. 5634–5643, Jul. 2018.

[29] A. Takahashi, A. Allam, and S. Onori, "Evaluating the feasibility of batteries for second-life applications using machine learning," *iScience*, vol. 26, no. 4, Apr. 2023, Art. no. 106547, doi: 10.1016/j.isci.2023.106547.

[30] C. Zhang, J. Jiang, W. Zhang, Y. Wang, S. Sharkh, and R. Xiong, "A novel data-driven fast capacity estimation of spent electric vehicle lithium-ion batteries," *Energies*, vol. 7, no. 12, pp. 8076–8094, Dec. 2014. [Online]. Available: https://www.mdpi.com/1996-1073/7/12/8076

[31] A. Bhatt, W. Ongsakul, N. Madhu, and J. G. Singh, "Machine learning-based approach for useful capacity prediction of second-life batteries employing appropriate input selection," *Int. J. Energy Res.*, vol. 45, no. 15, pp. 21023–21049, Dec. 2021.

[32] X. Li, Y. Dai, Y. Ge, J. Liu, Y. Shan, and L.-Y. Duan, "Uncertainty modeling for Out-of-Distribution generalization," 2022, *arXiv:2202.03958*.

[33] Y. Zhang, T. Wik, J. Bergström, M. Pecht, and C. Zou, "A machine learning-based framework for online prediction of battery ageing trajectory and lifetime using histogram data," *J. Power Sources*, vol. 526, Apr. 2022, Art. no. 231110.

[34] C. She, Y. Li, C. Zou, T. Wik, Z. Wang, and F. Sun, "Offline and online blended machine learning for lithium-ion battery health state estimation," *IEEE Trans. Transport. Electrific.*, vol. 8, no. 2, pp. 1604–1618, Jun. 2022.

[35] J. Zhou, D. Liu, Y. Peng, and X. Peng, "An optimized relevance vector machine with incremental learning strategy for lithium-ion battery remaining useful life estimation," in *Proc. IEEE Int. Instrum. Meas. Technol. Conf. (I2MTC)*, May 2013, pp. 561–565.

[36] Y. Xing, E. W. M. Ma, K. L. Tsui, and M. Pecht, "An ensemble model for predicting the remaining useful performance of lithium-ion batteries," *Microelectron. Rel.*, vol. 53, no. 6, pp. 811–820, Jan. 2013. [Online]. Available: https://www.sciencedirect.com/science/article/pii/S0026271412005227

[37] F. Von Bülow and T. Meisen, "State of health forecasting of heterogeneous lithium-ion battery types and operation enabled by transfer learning," in *Proc. PHM Soc. Eur. Conf.*, 2022, vol. 7, no. 1, pp. 490–508.

[38] S. Zhang, H. Zhu, J. Wu, and Z. Chen, "Voltage relaxation-based state-of-health estimation of lithium-ion batteries using convolutional neural networks and transfer learning," *J. Energy Storage*, vol. 73, Aug. 2023, Art. no. 108579.

[39] Y. Che, Y. Zheng, S. Onori, X. Hu, and R. Teodorescu, "Increasing generalization capability of battery health estimation using continual learning," *Cell Rep. Phys. Sci.*, vol. 4, no. 12, Dec. 2023, Art. no. 101743.

[40] W. Fan et al., "Enhancing capacity estimation of retired electric vehicle lithium-ion batteries through transfer learning from electrochemical impedance spectroscopy," *eTransportation*, vol. 22, Dec. 2024, Art. no. 100362. [Online]. Available: https://www.sciencedirect.com/science/article/pii/S2590116824000523

[41] J. Park, Y. Jin, W. Kam, and S. Han, "A practical semi-empirical model for predicting the SoH of lithium-ion battery: A novel perspective on short-term rest," *J. Energy Storage*, vol. 96, Aug. 2024, Art. no. 112659. [Online]. Available: https://www.sciencedirect.com/science/article/pii/S2352152X2402245X

[42] W. Xu et al., "Data-driven semi-empirical model approximation method for capacity degradation of retired lithium-ion battery considering SOC range," *Appl. Sci.*, vol. 13, no. 21, p. 11943, Oct. 2023.

[43] N. Jiang and H. Pang, "Study on co-estimation of SoC and SoH for second-use lithium-ion power batteries," *Electronics*, vol. 11, no. 11, p. 1789, Jun. 2022.

[44] X. Cui, M. A. Khan, S. Onori, G. Pozzato, S. Singh, and R. Sharma. (2024). *Stanford-Relyion Second-Life Li-Ion Battery Dataset*. Accessed: Nov. 17, 2024. [Online]. Available: https://osf.io/fns57/

[45] X. Cui, M. A. Khan, G. Pozzato, S. Singh, R. Sharma, and S. Onori, "Taking second-life batteries from exhausted to empowered using experiments, data analysis, and health estimation," *Cell Rep. Phys. Sci.*, vol. 5, no. 5, May 2024, Art. no. 101941.

[46] C. P. Aiken et al., "$Li[Ni_{0.5}Mn_{0.3}Co_{0.2}]O_2$ as a superior alternative to $LiFePO_4$ for long-lived low voltage Li-ion cells," *J. Electrochem. Soc.*, vol. 169, no. 5, 2022, Art. no. 050512.

[47] P. M. Attia et al., "'Knees' in lithium-ion battery aging trajectories," *J. Electrochem. Soc.*, vol. 169, no. 6, 2022, Art. no. 060517.

[48] X. Cui et al., "Lite-sparse hierarchical partial power processing for second-use battery energy storage systems," *IEEE Access*, vol. 10, pp. 90761–90777, 2022.

[49] X. Cui, A. Ramyar, J. B. Siegel, P. Mohtat, A. G. Stefanopoulou, and A.-T. Avestruz, "Comparing power processing system approaches in second-use battery energy buffering for electric vehicle charging," *J. Energy Storage*, vol. 49, May 2022, Art. no. 104017.